

JGR Space Physics

RESEARCH ARTICLE

10.1029/2019JA027321

Key Points:

- A SAR arc and diffuse aurora were simultaneously observed by all-sky imagers at two conjugate stations during the St. Patrick's Day storm in 2015
- Unlike diffuse aurora, SAR arc regions showed no significant increase of ionospheric scintillation indices or the rate of change of the TEC index (ROTI)
- Our observations at geomagnetic conjugate points suggest that SAR arcs cause no ionospheric irregularities affecting GPS signals, in contrast to effects at VHF

Supporting Information:

- Supporting Information S1
- Movie S1
- Movie S2
- Movie S3

Correspondence to:

Y. H. Kim,
yhkim@cnu.ac.kr

Citation:

Hong, J., Kim, J.-H., Chung, J.-K., Kim, Y. H., Kam, H., Park, J., & Mendillo, M. (2020). Simultaneous observations of SAR arc and its ionospheric response at subauroral conjugate points ($L \approx 2.5$) during the St. Patrick's Day Storm in 2015. *Journal of Geophysical Research: Space Physics*, 124. <https://doi.org/10.1029/2019JA027321>

Received 20 AUG 2019

Accepted 1 MAR 2020

Accepted article online 12 MAR 2020

Simultaneous Observations of SAR Arc and Its Ionospheric Response at Subauroral Conjugate Points ($L \approx 2.5$) During the St. Patrick's Day Storm in 2015

J. Hong^{1,2} , J.-H. Kim³ , J.-K. Chung² , Y. H. Kim¹ , H. Kam^{1,3}, J. Park^{2,4} , and M. Mendillo⁵

¹Department of Astronomy, Space Science and Geology, Chungnam National University, Daejeon, South Korea, ²Korea Astronomy and Space Science Institute, Daejeon, South Korea, ³Korea Polar Research Institute, Incheon, South Korea,

⁴Department of Astronomy and Space Science, Korea University of Science and Technology, Daejeon, South Korea,

⁵Center for Space Physics, Boston University, Boston, MA, USA in America

Abstract During the St. Patrick's Day storm on 17 March 2015, an all-sky imager at King Sejong Station (KSS; geo: 62.2°S, 58.8°W; mag: 50.2°S) captured diffuse aurora and a stable auroral red (SAR) arc. Ground-based Global Positioning System observations were also simultaneously conducted at KSS, but there was no significant increase in the total electron content's rate-of-change index or the ionospheric scintillation indices around the SAR arc region. Auroral activities including a SAR arc were also detected by the all-sky imager at Millstone Hill Station (geo: 42.6°N, 71.4°W; mag: 52.5°N), which is magnetically conjugate to KSS. The total electron content's rate-of-change index map around Millstone Hill Station, too, indicates that the ionospheric irregularities occurred only near the diffuse aurora and not in the SAR arc. The northern SAR arc is broader than the southern one and also shows a multiplicity pattern, which may be due to latitude structure within the seasonally dependent midlatitude ionospheric trough. These conjugate observations, despite their hemispheric differences, validate the classical SAR arc mechanism of emission driven by heat conduction from the inner magnetosphere that does not generate small-scale ionospheric irregularities that can affect Global Positioning System radio signals. Previous studies of SAR arcs and very high frequency radiowave scintillations did show a positive correlation.

1. Introduction

Stable auroral red (SAR) arcs have been studied for decades (Alexeyev et al., 2009; Baumgardner et al., 2007; Craven et al., 1982; Hoch, 1973; Kozyra et al., 1997; Rees & Roble, 1975) as a rarely observed optical phenomenon, which is seen in the subauroral ionosphere. They have purely red emission, are almost stationary, and can last for an entire night. The general mechanism for a SAR arc is well established (Rees & Roble, 1975, and references therein). When a geomagnetic storm occurs, the ring current strengthens and interacts with the plasmapause. Energetic protons of the ring current induce ion cyclotron wave turbulence, which dissipates approximately half the energy by Landau resonant interaction with the plasmaspheric electrons (Conrwall et al., 1971). Through thermal conduction along geomagnetic field lines connecting the ionosphere with the plasmasphere, the ionospheric electrons at F layer heights (~ 400 km) are heated to more than 3,000–4,000 K and collide with thermospheric oxygen atoms. The $O(^1D)$ atoms, which are excited by high-temperature electrons, radiate at the 630.0-nm wavelength. Because the number of electrons with kinetic energy greater than or equal to 4.12 eV is extremely small, emission of 557.7 nm from $O(^1S)$ is negligible. Thus, SAR arcs are spectrally pure redline emission. Damping of plasma waves such as ion cyclotron waves or kinetic Alfvén waves is also suggested for additional energy source as a SAR arc's long-lived emission (Kozyra et al., 1997). These processes mainly occur in the subauroral range of $2 < L < 4$, where the L value, introduced by McIlwain (1961), represents the set of geomagnetic field lines that cross the geomagnetic equator plane at L earth radii from the center of the Earth. However, the location of a SAR arc depends greatly on the magnitude of geomagnetic disturbance as characterized by the disturbance storm time (Dst) index (Kozyra et al., 1997). Kozyra et al. (1982) suggested that a SAR arc mainly occurs near the equatorward edge of the ionospheric trough where the electron density suddenly decreases. This reduced electron density region allows electron temperature to increase for a given heat flux from the magnetosphere.

SAR arc occurrence rates are also related to solar activity. Slater and Smith (1981) showed that SAR arc occurrence rates correlate well with sunspot number. Recently, Mendillo, Baumgardner, and Wroten (2016) established several categories of various SAR arc phenomena. They showed not only very long lasting SAR arcs but also multiple patterns, zonal/horizontal inhomogeneity, and geomagnetic tilts of SAR arc. Mendillo, Finan, et al. (2016) also described a rare kind of SAR arc that includes patches of green line emission induced by low energetic particle precipitation. Ongoing research deals with additional energy source mechanisms for SAR arcs, the influence of ring current evolution upon SAR arcs, and the roles of neutral composition and density.

Since a SAR arc is one of many ionospheric phenomena associated with severe ionospheric gradients, it is a possible site for ionospheric irregularities (see Kelly, 2009) that influence radio signals of the Global Positioning System (GPS) used for high precision geolocation. This practical reason is also a motivation to study SAR arc effects on the ionosphere.

One of the strongest geomagnetic storms in solar cycle 24 occurred in March 2015, known as St. Patrick's Day storm. Several studies (Cherniak & Zakharenkova, 2016; Liu et al., 2016; Ramsingh et al., 2015) investigated its effects on the Earth's ionospheric system from low- to high-latitude regions. Even though this geomagnetic storm was severe enough to affect midlatitude regions, there was no study to date about SAR arcs induced by this major storm. Here we report that SARs were simultaneously captured by a ground-based all-sky imager (ASI) at King Sejong Station (KSS) in Antarctica, as well as at its conjugate point in the northern hemisphere (Millstone Hill Station, MHS). GPS receivers in Antarctica and space-based data from the DMSP (Nichols, 1976) and Swarm satellites (Friis-Christensen et al., 2008) are used to describe the ionospheric patterns associated with this SAR arc.

2. Observations

The Korea Polar Research Institute has operated a KSS since 1989 in King George Island, Antarctica (geo; 62.2°S, 58.8°W/mag; 50.2°S). Being at a geomagnetically midlatitude location, KSS normally experiences no auroral activity under geomagnetically quiet conditions and very rarely phase scintillations of GPS signals. The ASI at KSS has been operated since 2008 to mainly investigate gravity waves in the mesosphere and lower thermosphere over the Antarctic peninsula. The ASI uses filters to obtain images at four airglow emission lines: O₂, OH, O (557.7 nm), and O (630.0 nm). During the 17 March 2015 storm, diffuse aurora and a SAR arc were imaged using the 630.0-nm emission line. The imaging was carried out with an exposure time of 150 s, and the observation cycle was about 5 min in order to include other emission lines and dark images. The observation schedule for the ASI depends on the location of the Sun and the Moon (to avoid disruption by lights from them). For this SAR arc, ASI observations started at 01:06 UT, 18 March. Observations ended at 03:07 UT due to an unexpected malfunction of the ASI. In general, the ambient 630.0-nm airglow emission is strongest at an altitude near 250 km, but SAR arcs occur at 400 km (Roach & Roach, 1963). Therefore, we projected the ASI images onto a geographical map at an altitude of 400 km in order to investigate the spatial characteristics of this SAR arc over KSS.

To assess ionospheric variations, we used observations of total electron content (TEC) made by a small network of GPS monitoring stations. Specifically, we used five stations south of the KSS site (see Movie S1 in the supporting information). Slant total electron content (STEC) values with elevation angle greater than 20° were used to calculate the rate of TEC (ROT) and rate of TEC index (ROTI) to monitor ionospheric irregularities, as described by Pi et al. (1997):

$$\text{ROT} = \frac{\text{STEC}_k^i - \text{STEC}_{k-1}^i}{t_k - t_{k-1}} \quad (1)$$

$$\text{ROTI} = \sqrt{\langle \text{ROT}^2 \rangle - \langle \text{ROT} \rangle^2} \quad (2)$$

where i and k are indices for the GPS satellite and time step, respectively. STEC, ROT, and ROTI values were computed every 30 s. ROTI values were derived as the standard deviation of ROT within a 5-min running window. As is the standard practice for GPS TEC data, we projected TEC patterns onto a plane at 350 km in altitude.

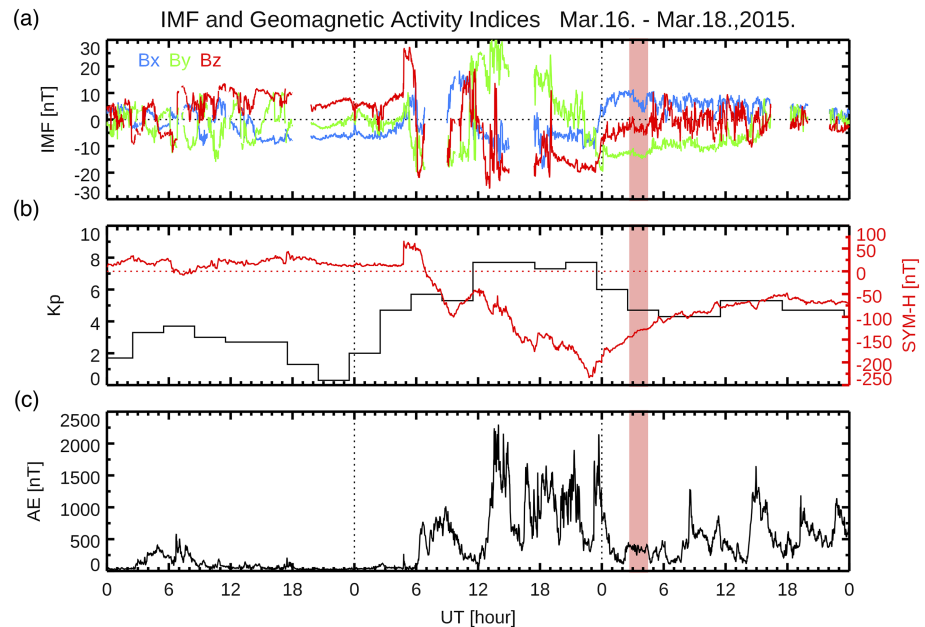


Figure 1. Geomagnetic activity indices from OMNI Web service during the St. Patrick's Day storm. (a) Three different colors indicate the three components of the interplanetary magnetic field (IMF), respectively. (b) Kp and SYM-H indices are represented in black and red lines, respectively. (c) The black line denotes the auroral electrojet (AE) index. The red shading indicates the period of the stable auroral red arc observed at King Sejong Station.

The northern hemispheric counterpart of the SAR arc was investigated by using ASI images at MHS, located close to the magnetic conjugate point (geo; 42.6°N, 71.4°W/mag; 52.5°N) of KSS. In addition, spaceborne data sets from the Swarm and Defense Meteorological Satellite Program (DMSP) satellites were utilized to inspect electron temperatures and energetic particle precipitation in the topside ionosphere.

3. Results

3.1. Geomagnetic Activity

Figure 1 presents solar wind and geomagnetic activity indices for 16–18 March 2015. In Figure 1a, the B_x and B_y components of the interplanetary magnetic field showed typical variations of a few nanotesla, while the B_z component was northward on 16 March. The B_z component abruptly increased and turned southward around 06 UT on 17 March and returned to northward around 10 UT. The interplanetary magnetic field B_z turned again to southward at ~12 UT and stayed southward until 03 UT (local midnight at KSS) on 18 March. In Figure 1b, SYM-H and Kp indices showed generally quiet conditions until 06 UT on 17 March when a sudden increase of the SYM-H index, corresponding to the storm sudden commencement, occurred. Shortly after the storm sudden commencement, the SYM-H index turned to negative, indicating the first main phase of the geomagnetic storm. The second main phase started at ~12 UT on 17 March, and the SYM-H index reached a minimum of -234 nT at 22:47 on 17 March. The Kp index started to increase at ~03 UT on 17 March and maintained high values of ~8 during the second main phase. In Figure 1c, the auroral electrojet (AE) index also showed very low values except at ~06 UT on 16 March, and then increased to ~1,000 nT during the first main phase, and exceeded 2,000 nT during the second main phase. After the second main phase, the recovery phase started and lasted for a few days. During the recovery phase, the AE index still showed active conditions of a few hundred nanotesla and Kp values were >4 .

3.2. SAR Arc Morphologies

The red shading in Figure 1 represents the period when the SAR arc was observed at KSS, that is, during the storm's recovery phase. Takagi et al. (2018) and prior studies have shown that a SAR arc typically starts to form during the recovery phase of a geomagnetic storm. Yet, as pointed out in Mendillo, Baumgardner, and Wroten (2016), improved detector capabilities reveal that SAR arcs can be observed closer to the

diffuse aurora, and thus much earlier in a storm—specifically during main phase onset. While the AE index decreased after 00:00 UT on 18 March, auroral activity had already expanded to near the KSS region. When KSS entered into the night-time sector, auroral 630.0-nm emission was actually observed over KSS (see Movie S1). Diffuse aurora started to be seen in the southern direction by KSS/ASI at 01:12 UT, and then covered most of the all-sky view over KSS. The SAR arc appeared over KSS at 01:39 UT. As time went by, the SAR arc feature was zonally elongated along a specific L-value line and increasingly more distinct in the ASI images. Auroral activity lasted steadily until 03:07 UT when, unfortunately, observation ended due to an unexpected malfunction of the ASI.

Based on the observation over MHS, the expanded diffuse auroral activity and SAR arc lasted longer than our observation over KSS. As evidence for that, the diffuse aurora and SAR arc were observed over MHS until around 06 UT (see Movie S2). The SAR arc over MHS, located close to the magnetic conjugate point of KSS, started to appear earlier than at KSS. The SAR arc already existed when the MHS/ASI started observation at 00:06 UT. The northern hemisphere SAR arc was somewhat broader in latitude and showed multiplicity patterns, one of the SAR arc types categorized by Mendillo, Baumgardner, and Wroten (2016). Although it became faint, it lasted until the end of the observations, at 09:47 UT. It is worth noting that the southern SAR arc started to appear about 1.5 hr or more later than the northern counterpart. In addition, the southern SAR arc was thinner and simpler than the northern one. In the supporting information, Movie S2 provides the full 10-hr data set from Millstone Hill.

Figures 2a and 2c show original 630.0-nm ASI images from KSS and MHS, respectively, taken near simultaneously at approximately 02:00 UT. In both ASI images, diffuse aurorae are clearly captured in poleward directions (south at KSS and north at MHS). The zonally extended emission features of the SAR arc are clearly seen equatorward, and considerably separated from, the diffuse aurora at both sites. Figures 2b and 2d are the projected ASI images over each station upon the 400-km altitude plane, together with several L-value lines shown in white. The yellow star in Figure 2b indicates the KSS's zenith, and the solid dot and the asterisk in Figure 2d mark the MHS's zenith and the conjugate point of KSS, respectively. The diffuse aurora shown in Figure 2b expanded to the southern corner of the projected plane, corresponding to the Antarctic peninsula where a network of GPS receivers is located. Note that the diffuse auroral boundary is actually closer to KSS than shown in the projected plane because diffuse auroral 630.0-nm emission mainly originates from the altitude of ~ 250 km. A distinct SAR arc shape can be seen from the north-east to south-west direction—equatorward of the auroral boundary. The north-east side of the SAR arc is well matched to the 2.5 L-value line, while the south-west side of the SAR arc is off from the 2.5 L-value line toward higher geomagnetic latitudes by ~ 0.15 L value. Similar features of the SAR arc can be seen in the MHS projected image.

To verify that the ASI observed feature was indeed a SAR arc, we have looked into corresponding spaceborne data sets. Figures 3a and 3b present energetic particle precipitation data measured by the DMSP satellite F19 in the northern and southern hemispheres, respectively. The F19 satellite passed the 2.5 L-value lines during the SAR arc period at geographic longitudes of 110°W and 80°E in the northern hemisphere and 60°E and 110°W in the southern hemisphere. Yet it is expected that a SAR arc induced by thermal heat conduction from enhanced ring current-plasmapause interactions will appear along the constant L-value footprints for a wide range of longitudes and thus be captured at the different longitude sectors sampled by the satellite. In Figure 3a, precipitations of energetic electrons and ions were recorded up to about 63 and 55°N in geomagnetic latitudes, respectively. These correspond to L values of about 5.49 and 3.45 at the DMSP altitude of 850 km, respectively. Similarly, energetic electrons and ions precipitations in the southern hemisphere had boundaries at about 54 and 57°S in geomagnetic latitude, equivalent to L values of about 3.28 and 3.82, respectively. Thus, there was no energetic particle (electron or ion) precipitation at the observed SAR arc region (~ 2.5 L value) in either hemispheres. As expected, energetic particle precipitations were detected at the higher latitude regions where diffuse aurora were observed by the ground-based ASIs.

Figure 3c presents electron temperatures (black line) and electron densities (red line) recorded by the Swarm B satellite at ~ 520 -km altitude. Swarm B passed to the west of the ASI observational coverage—close to 90°W during the SAR arc period. In the southern hemisphere, the electron temperature clearly increased to $4,000^\circ\text{K}$ around the observed SAR arc latitude. This is high enough to excite the atomic oxygen 630.0-nm emission. Electron densities conversely decreased in the SAR arc region. In the northern hemisphere, the

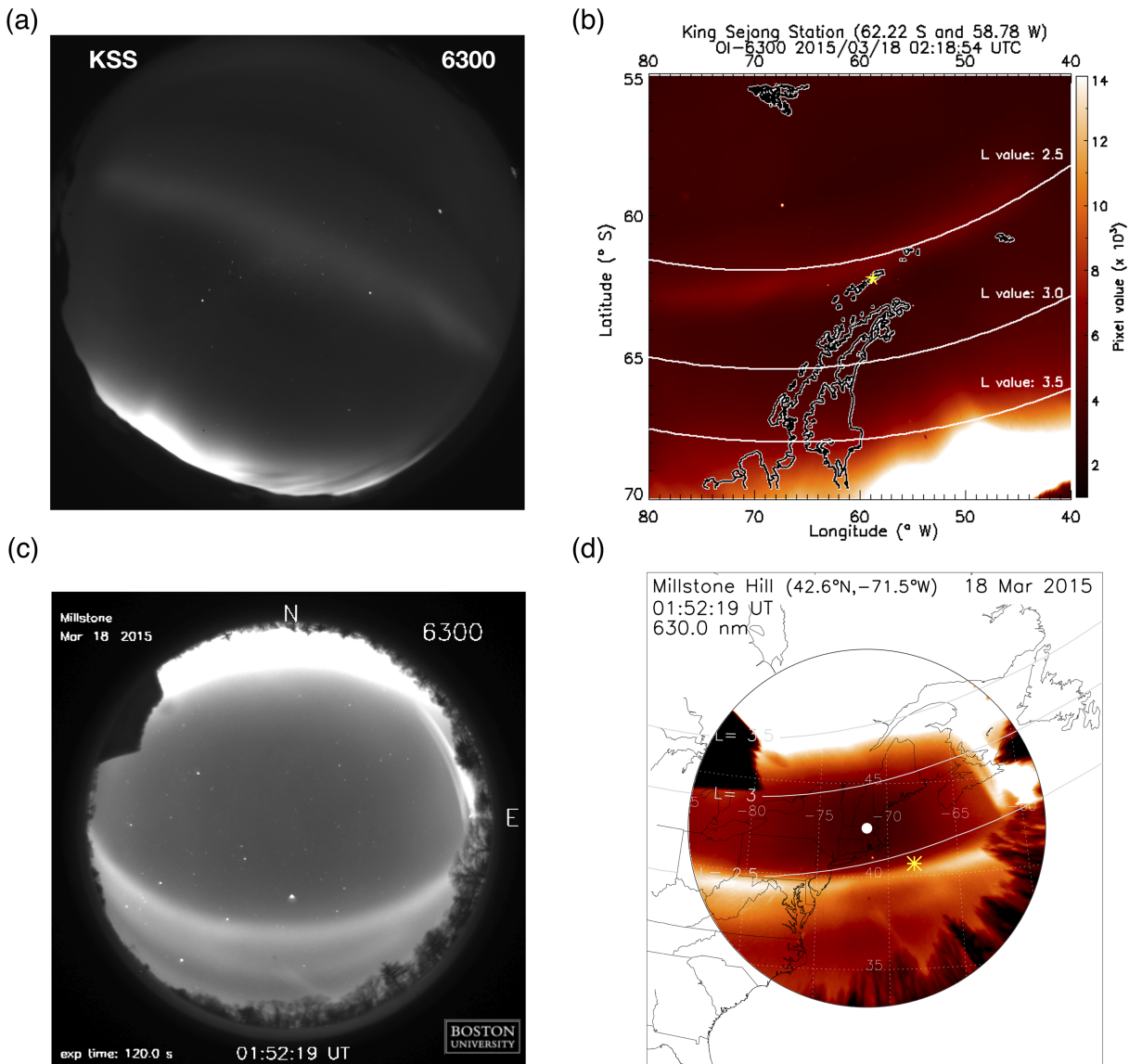


Figure 2. Simultaneous images of stable auroral red arc events observed by all-sky imagers at two magnetic conjugate points, King Sejong Station (KSS) and Millstone Hill Station (MHS). (a and c) Original images of atomic oxygen 630.0-nm emission over KSS and MHS, respectively. (b and d) Images portrayed geographically at a height of 400 km (the assumed altitude of stable auroral red arc emission). Brighter colors toward white indicate brighter 630.0-nm emission. The yellow star symbol in (b) denotes KSS. The white dot and yellow asterisk in (d) denote zenith at MHS and the conjugate point of KSS, respectively. Three white lines denote 2.5, 3.0, and 3.5 L-value lines at 400-km altitude calculated using altitude-adjusted corrected geomagnetic coordinates, respectively.

increase of electron temperature and the decrease of electron density are more dramatic. The electron densities around 03:24 UT (or 3.39 UT) suggest double minima within the region of elevated electron temperatures. By comparing the conjugate ASI images with the satellite measurements, we documented for the first time that different shapes of a SAR arc can occur due to variations in either or both the electron densities and temperatures. Overall, the measurements of DMSP and Swarm B clearly verified that the bright 630.0-nm arc features observed at the two conjugate points was the classic SAR arc phenomenon—emission from thermally excited atomic oxygen caused by heated ionospheric electrons and not due to particle precipitation.

3.3. Ionospheric Response to the SAR Arc

Ionospheric pierce points (IPPs) of two GPS satellites (designated PRN 3 and PRN 20) passed over the KSS region during the SAR arc period. Figure 4 compares the observed optical emissions with vertical TEC

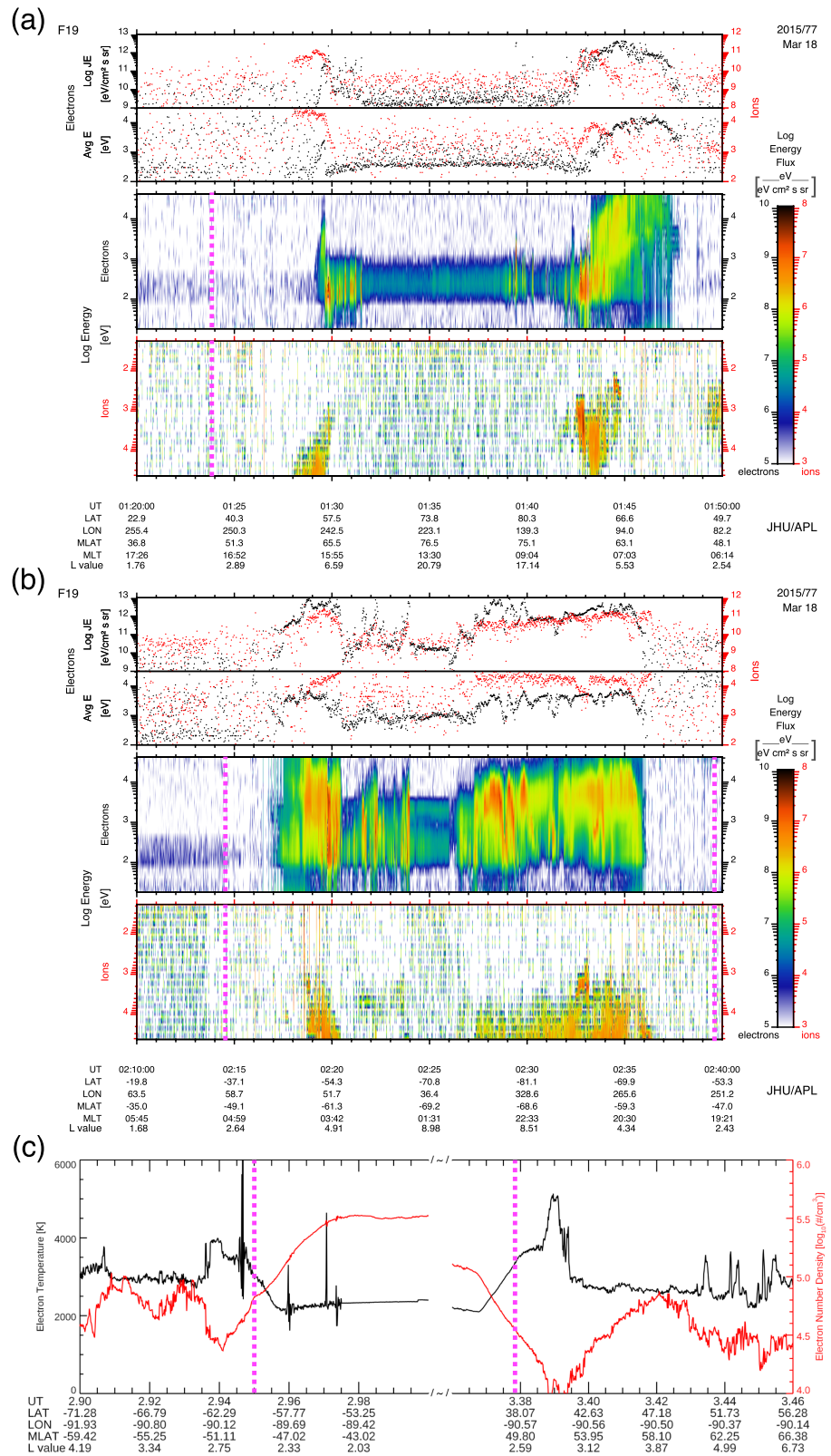


Figure 3. Energetic particle precipitations during the stable auroral red arc period recorded by DMSP satellite F19 in the (a) northern hemisphere and (b) southern hemisphere, respectively. (c) Electron temperature (black line) and electron density (red line) measured by Swarm B satellite. The vertical dashed lines (magenta) indicate 2.5 L value, the stable auroral red arc location.

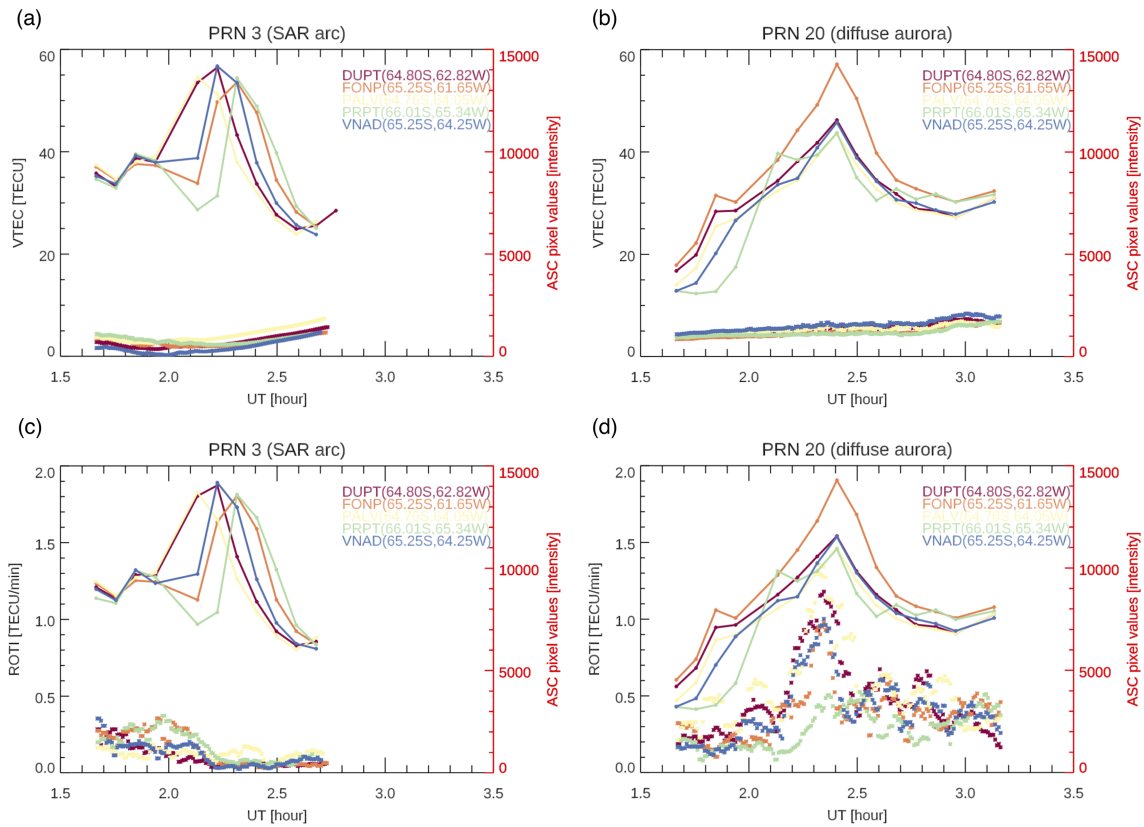


Figure 4. Vertical total electron contents (VTEC) and the rate of change of total electron content index (ROTI) from UNAVCO receivers and the brightness of atomic oxygen 630.0-nm emission corresponding to the locations of the satellites with respect to the images above King Sejong Station (KSS). The (a and b) VTEC and (c and d) ROTI are plotted by asterisk symbols. The left and right panels are for Global Positioning System satellites PRN 3 and PRN 20, whose lines of sight from the UNAVCO receivers traversed the SAR arc and diffuse aurora, respectively. Line plots in each panel represent relative values of OI 630.0-nm brightness corresponding to ionospheric pierce point of VTEC or ROTI. Five different colors indicate observations from the five UNAVCO stations.

(VTEC) and ROTI values along the ionospheric intersection/pierce points for five GPS receivers. Figures 4a and 4c show the observations made while crossing the SAR arc (PRN 3). Figures 4b and 4d show the data acquired while crossing the diffuse auroral boundary (PRN 20). The upper line plots in each panel represent relative values of OI 630.0-nm brightness (right axis units) along the tracks from the five receivers. In Figures 4a and 4b, 630.0-nm brightness values show drastic increases when the satellites cross the SAR arc and diffuse auroral boundary, respectively. In both cases, VTEC had characteristically low nighttime values, as shown by the lower lines in Figures 4a and 4b. Yet slight fluctuations of VTEC can be noticed when the IPPs of ray paths from PRN 20 crossed the diffuse auroral boundary near 02:30 UT in Figure 4b. This did not occur for VTEC observations when the IPPs of ray paths from PRN 3 crossed the SAR arc in Figure 4a.

The presence of strong ionospheric irregularities can be inferred using the ROTI values. In Figures 4c and 4d the ROTI values are presented for the SAR arc and diffuse aurora, respectively, along with the optical patterns in the top curves that are repeated from Figures 4a and 4b. Note that there are strong increases of ROTI in Figure 4d up to about 1.2 TEC unit/min near the diffuse aurora. This is consistent with previous studies (Jin et al., 2015; van der Meeren et al., 2015) that showed an association between diffuse auroral activity and the ionospheric-induced scintillation of GPS signals. On the other hand, there is no increase of ROTI when PRN 3 passed through the SAR arc region in Figure 4c. Furthermore, amplitude and phase scintillation indices (S_4 and σ_ϕ) for GPS signals measured by a GPS scintillation monitor [the Connected Autonomous Space Environment Sensor (CASES)] at KSS also did not detect any noteworthy features (not shown here).

4. Discussion

Unusually bright 630.0-nm emission was simultaneously detected by ASIs at both magnetic conjugate sites, KSS and MHS, respectively. A zonally stretched bright arc was seen along with strong diffuse aurora. The bright arcs captured by the ASI instruments at two conjugate points are confirmed as SAR arcs by DMSP and Swarm satellite over-flight observations. The SAR arc was well formed at the zenith of KSS, and it was stretched along $L = 2.5$, except in the south-west. Mendillo, Baumgardner, and Wroten (2016) reported five types of SAR arc including SAR arcs tilted with respect to geomagnetic latitude, and they suggested that the tilt of a SAR arc is due to distortion of the inner magnetospheric morphology under greatly disturbed geomagnetic conditions (as occurred with this St. Patrick's Day storm). Mendillo, Baumgardner, and Wroten (2016) also noted that tilted SAR arcs eventually returned to the normal pattern, that is, along a specific L-value line. Unfortunately, our ASI observation ended too early to ascertain whether the tilted SAR arcs return to a constant L-value line or not. On the other hand, the SAR arc over MHS shows not only tilted patterns but also multiplicity patterns that we relate to double electron density minima within a broad trough as shown in Figure 3c. The morphology differences in the two SAR arcs are consistent with seasonal differences between both hemispheres. Lower electron densities of the ionosphere during winter nighttime result in higher electron temperatures (Martinis et al., 2019). Even though the event occurred at the March equinox, the northern (southern) hemisphere was still in "ionospheric seasons" of winter (summer). As clearly captured by the Swarm satellite in Figure 3c, the background electron densities over MHS were lower than KSS, while the electron temperatures were higher over MHS than KSS. This feature is consistent with the hemispheric asymmetry of the SAR arc appearance times and widths.

The 630.0-nm emission originates from the transition of atomic oxygen's meta-stable state, $O(^1D)$ to the ground state, $O(^3P)$. The $O(^1D)$ state can be produced by direct excitation of atomic oxygen and dissociative excitation of molecular oxygen by energetic electrons (auroral region), and by direct excitation of atomic oxygen by thermal electrons found in SAR arcs (e.g., Schunk & Nagy, 2009). Normally, energetic electrons of 10^3 – 10^4 eV are precipitated into the auroral region and thermal electrons are produced in situ by thermal conduction from the plasmasphere. In the case of auroral precipitation, Kinrade et al. (2012) suggested that particle precipitation at the auroral boundary can cause plasma density irregularities of ~ 10 km in scale in the ionosphere. van der Meer et al. (2015) also investigated the relation between phase scintillation and auroral activity. Auroral precipitation has enough energy to excite atomic oxygen to the $O(^1D)$ state and also to ionize neutral species in the thermosphere. The highly structured increases in plasma density distribution resulting from spatially uneven auroral precipitation may trigger severe ionospheric scintillation. On the other hand, since thermal electrons cannot ionize neutral oxygen, no increase of plasma is expected, and thus, no significant ionospheric scintillation would occur in association with the 630.0-nm emission. In the ionospheric F layer at the plasmopause position, ionospheric electrons are heated by conduction via Coulomb collisions along the magnetic field and excite oxygen atoms to the $O(^1D)$ state (Rees & Roble, 1975). The fact that there was no auroral feature seen in 557.7-nm emission over KSS confirms that the energy associated with thermal heat conduction from the inner magnetosphere to the topside ionosphere is insufficient to cause electron density irregularities capable of causing scintillation in GPS signal data. This is in contrast to the rarer case of a SAR arc with structured patches of emission. Mendillo, Finan, et al. (2016) showed unusual SAR arcs that included regions of enhanced 630.0- and 557.7-nm emission that did exhibit GPS phase fluctuations. These resulted from low energetic particle precipitation due to inward motion of ring current particles (Shiokawa et al., 2013).

In this study, we reported that ROTI values, amplitude and phase scintillation indices for GPS signals, did not increase over the SAR arc observed by the ASI in KSS. Spaceborne measurements by Swarm and DMSP also confirm not only the absence of energetic particles but also the presence of electron density reductions and elevated electron temperatures within the SAR arc regions in both hemispheres. However, Basu (1974) and Aarons (1987) noted that the amplitude scintillation in very high frequency (VHF) radio signals (137 MHz) from satellite radio beacon measurements occurred in the SAR arc region. Such studies before the GPS era reported scintillations of VHF signals for satellite communication in the midlatitude trough that may or may not associate with SAR arcs (Aarons & Allen, 1971; Basu, 1978). The ROTI index refers to GPS phase fluctuations that are caused by kilometer-scale (or larger) irregularities, while the amplitude scintillations (via S_4 index) of a GPS signal are caused by much smaller scale irregularities (tens to

hundreds of meters). Since the reported VHF scintillations are due to small scale (~1 km to ~100 m) irregularities (Basu, 1978), the lack of GPS scintillations (in phase and amplitude) may imply that disturbances in the SAR arc region are not severe enough in the small-scale (sub-100 m) domain to interfere with GPS signals (L1: 1575.42 MHz, L2: 1227.60 MHz).

We also noted that ROTI values at the diffuse auroral boundary increased with the 630.0-nm emission brightness observed at KSS. In addition, the ROTI maps over North America provided by the National Institute of Information and Communications Technology also indicated distinct increases of ROTI values only near the diffuse auroral region, the northern part of images from MHS (not shown here but see Movie S3). The DMSP data also showed significant energetic particle fluxes in the diffuse auroral regions observed by ASIs in KSS and MHS. Thus, our study demonstrates that the SAR arc did not cause GPS scintillations due to the absence of particle precipitation, unlike the diffuse auroral region.

5. Conclusions

We observed simultaneous SAR arcs with ASIs at KSS and MHS, magnetic conjugate points, during the St. Patrick's Day storm in 2015. We noted neither significant GPS scintillation nor significant increase of ROTI values in the SAR arcs over KSS and MHS. In contrast, ROTI values were enhanced significantly in the accompanied diffuse aurora over both conjugate points. This implies that SAR arcs are generated by thermal conduction from the plasmaspheric ring current during geomagnetic storms, according to the classical mechanism of SAR arc formation, which does not cause significant ionospheric plasma density irregularities. The fact that no significant 557.7-nm emission from the arc was detected at both sites further strengthens the thermal conduction argument, rather than low energy precipitation, which occurs in rare cases of SAR arcs accompanied with GPS phase fluctuation. Along with satellite measurements, our study observationally confirmed the classical mechanism of SAR arc generation and found that it does not lead to scintillation of GPS signals in the L band (1–2 GHz). However, SAR arcs may cause scintillation in the VHF band (30–300 MHz) as other studies reported, suggesting a size dependency of irregularities in SAR arcs. We also found hemispheric differences in the SAR arcs: the northern arc showed a broader latitudinal extent and multiplicity patterns due to structures within the background electron density in the broader midlatitude trough in winter. Further studies are needed to understand the overall pattern of ionospheric irregularities for various types and cases of SAR arcs, in association of 557.7-nm emission and VHF versus GPS signal fluctuations.

References

- Aarons, J. (1987). F layer irregularity observations of the SAR arc event of March 5–6, 1981. *Radio Science*, 22, 100–110. <https://doi.org/10.1029/RS022i001p00100>
- Aarons, J., & Allen, R. S. (1971). Scintillation boundary during quiet and disturbed magnetic conditions. *Journal of Geophysical Research*, 76, 170–177. <https://doi.org/10.1029/JA076i001p00170>
- Alexeyev, V., Ievenko, I., & Parnikov, S. (2009). Occurrence rate of SAR arcs during the 23rd solar activity cycle. *Advances in Space Research*, 44, 524–527. <https://doi.org/10.1016/j.asr.2009.04.024>
- Basu, S. (1974). VHF ionospheric scintillation at L = 2.8 and formation of stable auroral red arcs by magnetospheric heat conduction. *Journal of Geophysical Research*, 79, 3155–3160. <https://doi.org/10.1029/JA079i022p03155>
- Basu, S. (1978). Ogo 6 observations of small-scale irregularity structures associated with subtrough density gradients. *Journal of Geophysical Research*, 83, 182–190. <https://doi.org/10.1029/JA083iA01p00182>
- Baumgardner, J., Wroten, J., Semeter, J., Kozyra, J., Buonsanto, M., Erickson, P., & Mendillo, M. (2007). A very bright SAR arc: Implications for extreme magnetosphere-ionosphere coupling. *Annales Geophysicae*, 25, 2593–2608. <https://doi.org/10.5194/angeo-25-2593-2007>
- Cherniak, I., & Zakharenkova, I. (2016). High-latitude ionospheric irregularities: Differences between ground- and space-based GPS measurements during the 2015 St. Patrick's Day storm. *Earth, Planets and Space*, 68(1), 1–13. <https://doi.org/10.1186/s40623-016-0506-1>
- Conrall, J. M., Coroniti, F. V., & Thorne, R. M. (1971). Unified theory of SAR arc formation at the plasmapause. *Journal of Geophysical Research*, 76, 4428–4445. <https://doi.org/10.1029/JA076i019p04428>
- Craven, J. D., Frank, L. A., & Ackerson, K. L. (1982). Global observations of a SAR arc. *Geophysical Research Letters*, 9, 961–964. <https://doi.org/10.1029/GL009i009p00961>
- Friis-Christensen, E., Lühr, H., Knudsen, D., & Haagmans, R. (2008). Swarm—An Earth observation mission investigating geospace. *Advances in Space Research*, 41, 210–216. <https://doi.org/10.1016/j.asr.2006.10.008>
- Hoch, R. J. (1973). Stable auroral red arcs. *Reviews of Geophysics*, 11(4), 935–949. <https://doi.org/10.1029/RG011i004p00935>
- Jin, Y., Moen, J. I., & Miloch, W. J. (2015). On the collocation of the cusp aurora and the GPS phase scintillation: A statistical study. *Journal of Geophysical Research: Space Physics*, 120, 9176–9191. <https://doi.org/10.1002/2015JA021449>
- Kelly, M. C. (2009). *The Earth's ionosphere: Plasma physics and electrodynamics*. Amsterdam: Academic Press, Elsevier.
- Kinrade, J., Mitchell, C. N., Yin, P., Smith, N., Jarvis, M. J., Maxfield, D. J., et al. (2012). Ionospheric scintillation over Antarctica during the storm of 5–6 April 2010. *Journal of Geophysical Research*, 117, A05304. <https://doi.org/10.1029/2011JA017073>

Acknowledgments

This work is supported by the basic research fund from Korea Astronomy and Space Science Institute (2020185005), and it is also assisted by research program from the Korea Polar Research Institute (PE20100). All-sky images from King Sejong Station can be accessed from <https://kpsc.kopri.re.kr/>. All-sky-images from Millstone Hill appear at the Boston University website <http://sirius.bu.edu/data/>, supported by a grant from the Aeronomy Program at the U.S. National Science Foundation. Geomagnetic indices are obtained from NASA OMNI Web service <https://omniweb.gsfc.nasa.gov/form/dx1.html>. UNAVCO RINEX data are downloaded in UNAVCO data archive <https://www.unavco.org/data/gps-gnss/data-access-methods/dai2/app/dai2.html#>. Defense Meteorological Satellite Program (DMSP) plots are conducted by JHU/APL software supported in its website <http://sd-www.jhuapl.edu/Aurora/data/app/DMSP.jnlp>. Swarm satellite data are provided in European Space Agency (ESA) website <http://swarm-diss.esa.int/>. Supporting information of ROTI maps over northern American sector are obtained from National Institute of Information and Communications Technology (NICT) website http://seg-web.nict.go.jp/GPS/N_AMRC/RMAP/.

- Kozyra, J. U., Cravens, T. E., Nagy, A. F., Chandler, M. O., Brace, L. H., Maynard, N. C., et al. (1982). Characteristics of a stable auroral red arc event. *Geophysical Research Letters*, *9*, 973–976. <https://doi.org/10.1029/GL009i009p00973>
- Kozyra, J. U., Nagy, A. F., & Slater, D. W. (1997). High-altitude energy source(s) for stable auroral red arcs. *Reviews of Geophysics*, *35*, 155–190. <https://doi.org/10.1029/96RG03194>
- Liu, J., Wang, W., Burns, A., Yue, X., Zhang, S., Zhang, Y., & Huang, C. (2016). Profiles of ionospheric storm-enhanced density during the 17 March 2015 great storm. *Journal of Geophysical Research: Space Physics*, *121*, 727–744. <https://doi.org/10.1002/2015JA021832>
- Martinis, C., Baumgardner, J., Mendillo, M., Taylor, M. J., Moffat-Griffin, T., Wroten, J., et al. (2019). First ground-based conjugate observations of stable auroral red (SAR) arcs. *Journal of Geophysical Research: Space Physics*, *124*, 4658–4671. <https://doi.org/10.1029/2018JA026017>
- McIlwain, C. E. (1961). Coordinates for mapping the distribution of magnetically trapped particles. *Journal of Geophysical Research*, *66*, 3681–3691. <https://doi.org/10.1029/JZ066i011p03681>
- Mendillo, M., Baumgardner, J., & Wroten, J. (2016). SAR arcs we have seen: Evidence for variability in stable auroral red arcs. *Journal of Geophysical Research: Space Physics*, *121*, 245–262. <https://doi.org/10.1002/2015JA021722>
- Mendillo, M., Finan, R., Baumgardner, J., Wroten, J., Martinis, C., & Casillas, M. (2016). A stable auroral red (SAR) arc with multiple emission features. *Journal of Geophysical Research: Space Physics*, *121*, 10,564–10,577. <https://doi.org/10.1002/2016JA023258>
- Nichols, D. A. (1976). DMSP Block-5A, B, C Compendium, Space Division/YDE, U.S. Air Force, Weather Service, Los Angeles, Calif.
- Pi, X., Mannucci, A. J., Lindqwister, U. J., & Ho, C. M. (1997). Monitoring of global ionospheric irregularities using the worldwide GPS network. *Geophysical Research Letters*, *24*, 2283–2286. <https://doi.org/10.1029/97GL02273>
- Ramsingh, S., Sripathi, S., Sreekumar, S., Banola, K., Emperumal, P. T., & Kumar, B. S. (2015). Low-latitude ionosphere response to super geomagnetic storm of 17/18 March 2015: Results from a chain of ground-based observations over Indian sector. *Journal of Geophysical Research: Space Physics*, *120*, 864–10,882. <https://doi.org/10.1002/2015JA021509>
- Rees, M. H., & Roble, R. G. (1975). Observations and theory of the formation of stable auroral red arcs. *Reviews of Geophysics*, *13*, 201–242. <https://doi.org/10.1029/RG013i001p0201>
- Roach, F. E., & Roach, J. R. (1963). Stable 6300 Å auroral arcs in mid-latitude. *Planetary and Space Science*, *11*, 523–545. [https://doi.org/10.1016/0032-0633\(63\)90076-X](https://doi.org/10.1016/0032-0633(63)90076-X)
- Schunk, R. W., & Nagy, A. F. (2009). *Ionosphere: Physics, Plasma Physics, and Chemistry*. New York: Cambridge University Press.
- Shiokawa, K., Miyashi, Y., Brandt, P., Evans, D., Frey, H., Goldstein, J., & Yumoto, K. (2013). Ground and satellite observation of low-latitude red auroras at the initial phase of magnetic storms. *Journal of Geophysical Research: Space Physics*, *118*, 256–270. <https://doi.org/10.1029/2012JA018001>
- Slater, D. W., & Smith, L. L. (1981). Modulation of stable auroral red (SAR) arc occurrence rates. *Journal of Geophysical Research*, *86*, 3669–1673. <https://doi.org/10.1029/JA086iA05p03669>
- Takagi, Y., Shiokawa, K., Otsuka, Y., Connors, M., & Schofield, I. (2018). Statistical analysis of SAR arc detachment from the main oval based on 11-year, all-sky imaging observation at Athabasca, Canada. *Geophysical Research Letters*, *45*, 11,539–11,546. <https://doi.org/10.1029/2018GL079615>
- van der Meer, C., Oksavik, K., Lorentzen, D. A., Rietveld, M. T., & Clausen, L. B. N. (2015). Severe and localized GNSS scintillation at the poleward edge of the nightside auroral oval during intense sub-storm aurora. *Journal of Geophysical Research: Space Physics*, *120*, 10,607–10,621. <https://doi.org/10.1002/2015JA021819>